The cortical microtubules of *Toxoplasma* contribute to the helicity, but not the speed or persistence of parasite movement

Isadonna F. Tengganu[1#], Luisa F. Arias Padilla[1#], Jonathan Munera Lopez[1#], Jun Liu[2,3], Peter T. Brown[4], Ke Hu[1*]

[1]Biodesign Center for Mechanisms of Evolution/School of Life Sciences, Arizona State University, USA
[2]Department of Biology, Indiana University, USA; [3]Current address: Berkgen Biopharmaceuticals, Shenzhen, China
[4]Department of Physics and Center for Biological Physics, Arizona State University, USA

#: equal contribution

**: Address correspondence to:*
Email: kehu4@asu.edu

Running title: *cortical microtubules facilitate helical parasite movement*

ABSTRACT

Apicomplexans parasitize a wide range of hosts. To infect, the parasite needs to travel through different types of tissues and invade into various types of cells. In tissues and three-dimensional (3-D) matrix, the apicomplexan parasite *Toxoplasma gondii* moves along a helical path. While many genes, including actin and myosins, have been shown to be important for parasite motility, it remains unknown what allows the parasite to travel over a long distance along a helical path. The cortical microtubules, which are ultra-stable, sprially arranged, and form extensive lateral interaction with the parasite cortex, have been considered to be a candidate structure for guiding the long-distance movement of the parasite.

In wild-type parasites, the cortical microtubules in mature parasites are impervious to destabilization by cold-treatment or depolymerizing drugs, which makes it difficult to assess their function. Previously, we generated a mutant (dubbed "TKO" for succinctness) that lacks three microtubule-associated proteins. The loss of these three proteins destabilizes the cortical microtubules in mature parasites. Here we quantify the proportion of parasites with various levels of defects in the microtubule array under different conditions. We found that ~ 80% of the non-dividing TKO parasites have severely curtailed cortical microtubules. The extent of depolymerization is further exacerbated upon the initiation of daughter construction or cold treatment. The cold-induced depolymerization is reversible, with noticeable restoration of the cortical microtubules within 20 min of temperature shift to 37°C. While microtubule polymerization is essential for generating viable daughter cells, the destabilization of the cortical microtubules in the mature parasite does not affect parasite replication. In a 3-D Matrigel matrix, the TKO mutant parasites can travel directionally over long distances. However, their trajectories are significantly more linear than those of wild-type parasites. In tissue culture, the TKO parasite displays a defect in infection and cytolytic efficiency. Interestingly, the speed and behavior of the parasite's entry into and egress from the host cell are similar to that of the wild-type parasite. These results indicate that the cortical microtubules contribute to the helicity but not the persistence of parasite long-distance movement. Furthermore, host cell entry is less sensitive to structural changes in the parasite than overall infection efficiency, which also include extracellular migration and orient the parasite for proper contact with the host cell.

INTRODUCTION

Apicomplexans are obligate intracellular parasites, many of which are important pathogens. For example, the malaria parasites, *Plasmodium* spp., kill more than half a million people each year [1]. *Toxoplasma gondii* permanently infects ~ 20% of the global human population and can infect any warm-blooded animal [2]. As obligate intracellular organisms, a successful infection requires the parasite to travel over a long distance through tissues with varying biochemical and biophysical properties as well as to enter into host cells, which requires shorter travel distance, but perhaps more finesse, as the host cell plasma membrane needs to remain intact to allow the parasite to use host cell resources for proliferation.

Toxoplasma gondii moves along an irregular helical path in tissues and a three-dimensional (3-D) matrix over tens of microns [3]. Chemical inhibition as well as genetic manipulations showed that the basic components driving the motility of *Toxoplasma* include actin and a series of apical and cortical myosin motors for providing the driving force, secreted adhesins on the parasite surface for engaging with the environment, as well as associated proteins for coupling the intracellular domains of the adhesins to the actomyosin complex [4-13]. The characterization of these players has significantly advanced the understanding of how energy is injected into the system to fuel motility. However, while actin polymerization is critical for parasite movement, no native actin filaments have been detected, suggesting that the polymerization is likely to occur dynamically. Thus, it is still not known how the parasite is capable of traveling over long distance along a helical path. Intuitively, a stable, inherently helical cortical structure would be required for guiding continuous parasite movement over a long distance.

In *Toxoplasma,* one of the main cytoskeletal structures with a roughly helical arrangement is the set of cortex-associating (denoted as "subpellicular" or "cortical") microtubules that are anchored at one end in a ring-like structure (the apical polar ring) at the parasite apex [14-16]. Among the apicomplexans, the microtubule cytoskeleton displays intriguing species and life-stage specific variations that coincide with substantial differences in physiology. The mature *Plasmodium* ookinete has an intricate cage of ~ 60 cortical microtubules [17-19], but the asexual blood-stage parasites only have a narrow band of 2-4 cortical microtubules that extends down one side of the parasite [14, 20]. The *Toxoplasma* tachyzoite has consistently 22 cortical microtubules that are arranged in a helical, or more accurately, a spiral pattern. The parasite invests considerable amount of resources in building and maintaining these polymers. Aside from the core building blocks, the tubulins, there is a suite of proteins that associate with the cortical microtubules in a region-specific manner [15, 21-23]. In mature parasites, these microtubules form an ultra-stable "rib cage" that form extensive lateral interaction with the inner membrane complex (IMC). They remain intact under treatments that depolymerize microtubules in mammalian cells within minutes [24, 25]. This extraordinary stability makes it difficult to assess the function of these polymers in the mature parasite.

Previously, we generated a mutant (dubbed "TKO" for succinctness) that lacks three microtubule-associated proteins, TLAP2, SPM1 and TLAP3 [22]. The removal of these three proteins dramatically reduces the stability of the cortical microtubules in mature parasites. In the present work, we quantified the proportion of parasites with various levels of defects in the microtubule array under different conditions and found that ~ 80% of the non-dividing TKO parasites have severely curtailed cortical microtubules. Depolymerization in mature parasites becomes even more pronounced upon the initiation of daughter construction or cold treatment,

the latter effect being reversible. While microtubule polymerization is essential for generating viable daughter cells, parasite replication is not affected by the destabilization of the cortical microtubules in the mature parasite. In a 3-D Matrigel matrix, the TKO mutant parasite moves as persistently as the wild-type parasite with similar velocity and net displacement. However, it travels along a path significantly more linear than the wild-type parasite. Interestingly, even though the cytolytic efficiency of the TKO parasite is significanty lower, live cell imaging revealed that the parasite's behaviors during entry into and egress from the host cell is indistinguishable from those of the wild-type. These results indicate that the cortical microtubules contribute to the helicity but not the persistence of parasite long-distance movement. On the other hand, host cell entry and egress, which involve short-distance travel, is less sensitive to structural changes in the parasite than overall infection efficiency.

RESULTS

The TKO parasite replicates normally, likely due to the cell-stage dependent nature of the destabilization of cortical microtubules

Previously, we showed qualitatively that the cortical microtubules in mature TKO parasites are destabilized compared with those in the wild-type parasites [22]. Here to quantify the extent of destabilization, we determined the proportions of TKO and wild-type parasites that display various characteristics in the microtubule array. We found that the cortical microtubules are severely curtailed in 79% (±8.5% SEM) of non-dividing TKO parasites and sparse in the rest, whereas 100% of the wild-type parasites have a full, regularly arranged array (Fig 1A) (Three independent experiments, total 490 parasites analyzed for the TKO and 246 parasites analyzed for the wild-type). The extent of depolymerization in mature TKO parasites is more pronounced during cell division (Fig 1B-C). The proportion of parasites with nearly fully depolymerized cortical microtubules ("absent" category) was ~ 42% at the initiation stage of daughter construction and increased to ~ 98% prior to daughter emergence from the mother parasite (Fig 1C). For wild-type parasites, the cortical microtubules of the mother parasite in the initiation and elongation stages of daughter construction are similar to that of non-dividing stage (Fig 1B-C). However, ~ 24% of mature parasites at the pre-emergence stage and 100% during daughter emergence have short microtubules.

We examined the average number of rounds of replication at 12, 24, and 36 hours after infection and found that the rate of replication of the TKO parasite is very similar to that of the wild-type parasite (Fig 1D). At first glance, it is surprising that a mutant that has destabilized cortical microtubules does not have a replication defect, because microtubule polymerization is coupled with cortex formation, and thus is required for the daughter formation [26-29]. However, as we observed previously [22], in the same cell in which the cortical microtubules of the mother TKO parasite are depolymerized, the microtubules do polymerize in growing daughters, which develop normally. These results reveal a cell-stage dependent microtubule depolymerizing activity that acts on the cortical microtubules in mature parasites but not the polymerizing microtubules in growing daughters. The depolymerization of cortical microtubules in mature TKO parasites becomes apparent at a much earlier stage and is much more complete than the wild-type parasites likely because they are already destabilized due to the lack of TLAP2, TLAP3, and SPM1.

In our previous work, we showed that incubation at ~ 8°C can further destabilize the cortical microtubules of the TKO parasite [22]. Here we characterize the time course of cold-

160 induced disassembly of cortical MTs in mature TKO parasites and found that, as expected, the
161 extent of depolymerization increased with time of cold-treatment (Fig 1E). After ~ 2 hr of cold-
162 treatment (C120), cortical MTs in ~ 72% of the parasites are nearly completely depolymerized
163 with no visible MTs aside from a small tubulin-positive "cap" at the apical end ("absent"
164 category). On the other hand, the array of cortical microtubules in wild-type parasite remains
165 similar before and after the cold treatment. The cold-induced depolymerization in the TKO
166 parasite is reversible (Fig 1E). When TKO cultures cold-treated for 2 hr were returned to 37°C,
167 the cortical MTs were restored significantly after 20 min of the temperature shift. At 1hr of 37°C
168 incubation (R60), ~ 80% of the parasites showed patterns ("short or sparse") similar to those of
169 untreated parasites, with the microtubules concentrated at the apical end of the parasite (Fig
170 3E), suggesting strong preference for elongation from pre-existing nucleation sites.
171
172
173 *The trajectory of movement of TKO parasite is more linear than that of the wild-type parasite in*
174 *3-D matrigel*
175
176 In wild-type parasites, the stable, spirally arranged cortical microtubules have been proposed
177 to guide directionality of parasite movement [30] or to function as a spring that transmits
178 energy to drive gliding motility [31]. We tested this hypothesis by comparing the 3-D motile
179 behaviors of the wild-type parental with those of the TKO parasite, taking advantage of the
180 destabilized and curtailed microtubule array in the TKO. By modifying an established Matrigel-
181 based 3-D motility assay [3], we obtained optical sections of the moving parasites under a
182 label-free condition through Differential Interference Contrast (DIC) imaging. DIC imaging not
183 only minimizes phototoxicity, but also enables the observation of parasite morphological
184 changes as they move. However, while fluorescence images exhibit high-contrast that
185 facilitates cell-tracking, computerization of cell positions in DIC image stacks are not as
186 straightforward. We applied a series of edge detection filters, followed by erosion and dilation
187 filters on the DIC images to derive images with contrast similar to fluorescence images (Fig
188 2A-B) that are amenable to 3-D cell tracking. Detection and tracking were carried out using the
189 TrackMate plugin in Fiji which generates the 3-D coordinates of the cell trajectories for further
190 analysis and 3-D visualization (Fig 2C and Fig 3, Video S1-S4).
191
192 In these experiments, 40.2% of the wild-type parental (RH*Δhx*) parasites were motile
193 (413 parasites from 6 independent experiments analyzed) (Table 1). The average net
194 displacement is 31.4 μm. The average run length (i.e., distance between pauses of >5.4 sec)
195 is 22.7 μm and the average run speed (average speed during a run) is 1.28 μm/sec (Fig 3A).
196 Similarly, ~42.3% of the TKO parasites were motile (395 parasites from 6 independent
197 experiments analyzed) with an average net displacement of 31.8 μm, average run length of
198 23.3 μm and average run speed of 1.3 μm/sec. As previously reported [3], the wild-type
199 parasite moves along an irregular helical path. The average dispersal ratio (ratio of net
200 displacement to total distance traveled of motile segments) of the trajectories is 0.71(a value of
201 1 indicates a completely linear track). The average turn angle (relative angle of parasite
202 between two consecutive steps) is ~50°. The movement of the TKO parasite was visibly more
203 linear than that of the wild-type parasite (Fig 3B, Video S1-S2). Confirming this visual
204 impression, we found that the dispersal ratio of the TKO parasites is 0.78, significantly higher
205 than that of the wild-type parasite ($p << 0.0001$, Fig 3C). The turn angle of the TKO is ~32.6°,
206 significantly lower than the wild-type parasite ($p << 0.0001$). Both are consistent with the
207 trajectories being more linear. For segments of trajectories during which the TKO parasite
208 displays near helical movement, the average pitch of the helical turns is 9.9 μm, significantly
209 higher than that of the wild-type parasite, which is 7.5 μm ($p << 0.0001$).

As shown in Figure 1A, there are remnant cortical microtubules in untreated TKO parasites. To determine whether these remaining microtubules influence parasite movement, we cold-treated the parasites for 2 hr, under which condition the cortical microtubules are nearly fully depolymerized in >70% of the TKO parasites but those in the wild-type parasites are not affected (see Fig 1E). The parasites were then harvested and mixed with Matrigel for 3-D motility assay. We found that the trajectories of the cold-treated TKO parasites are qualitatively similar to those of untreated TKO parasites (Fig 3B).

In addition to the cortical microtubules, another helically arranged cytoskeletal structure in the parasite is the conoid (Fig 1B), which is a substructure in the apical complex formed of helically arranged tubulin fibers [25, 28, 32, 33]. When a structural component (TgDCX) was removed, the conoid structure becomes stunted and disorganized and the parasite displays severe invasion defects [33]. To determine whether the helicity of the trajectory is sensitive to changes in the conoid structure, we examined the motile behavior of the DCX knockout parasite (*Δdcx*). We found that on average, the motile percentage of the *Δdcx* is ~31%, slightly lower than that of its "wild-type" parental (RH*Δhx*Δ*ku80*, abbreviated as "RH*Δku80*") (Table 1). The average net displacement, run-length and run speed of the *Δdcx* parasite are similar to those of the wild-type parasites (30.2 vs 30.7 μm, ~26 vs 25 μm and 1.21 vs 1.28 μm/sec, respectively, Fig 3A). The trajectories of the *Δdcx* are helical in nature (Fig 3B-C, Video S3-S4), with an average dispersal ratio of 0.68 and turn angle of 52°, indicating slightly tighter turns compared with its parental parasite (average dispersal ratio of 0.72 and turn angle of 48.4°, $p < 0.05$, Fig 3C). This indicates that the conoid is not a major contributor to the helicity of parasite movement.

The infection efficiency of the TKO is lower than that of the wild-type parasite, while entry into and calcium-induced egress from the host cell are not affected

Parasite motility is critical for invasion into and egress from the host cell [4-9, 12, 13, 34]. In addition, as the cortical microtubules are stable polymers that associate extensively with the parasite cortex, it is conceivable that they might provide mechanical support to the cortex when the parasites penetrate the membrane of the host cell during entry or exit. We therefore used video microscopy to determine whether the destabilization of the cortical microtubules in the TKO parasite might affect any of these processes. To examine parasite egress, the cultures infected by TKO or RH*Δhx* (wild-type parental) parasites were subjected to cold-treatment for 1 hr and then placed at 37°C for egress induced by the calcium ionophore A23187. Both TKO and wild-type parasites egressed actively and efficiently (Fig 4A, Video S5). Within ~ 1 min, egress was completed in >93% of vacuoles for the wild-type parasites (n=15) and in 100% of vacuoles for the TKO parasites (n=15) (Fig 4B).

To assess the parasite behavior during entry into the host cell, freshly harvested extracellular parasites were settled onto the host cell monolayer by a ~ 10 min pre-incubation on ice and then imaged by DIC at 37°C (Fig 4C, Video S6). The number of entry events was recorded for four parasite lines: wild-type RH∆*hx* parental, TKO, wild-type RH∆*hx*∆*ku80* parental, and *Δdcx* parasite. We observed 58 events for RH∆*hx* in 10 videos, 40 for TKO in 13 videos, 56 for RH∆*ku80* in 9 videos, and 35 for ∆*dcx* in 22 videos. The median speed of host cell entry was 25.5 second for RH∆*hx*, 22.5 second for the TKO, 25 second for the RH∆*hx*∆*ku80* and 33 second for the ∆*dcx* parasites (Fig 4D). We also did not observe any notable differences in morphological changes (*e.g.* the formation and resolution of constrictions) during host cell entry among these parasite lines.

The lower incidence of entry attempts observed in the time-lapse experiments for the TKO and Δ*dcx* indicates lower overall infection efficiency. Indeed, Δ*dcx* parasite was shown in our previous work to invade at ~ 25% of the efficiency of the wild-type parasites when assessed by an immunofluorescence based assay [33]. Consistent with lower efficiency in infection, the TKO parasite generates ~ 60% of the number of plaques as the wild-type parasite ($p \approx 0.005$) when examined by the plaque assay, where the parasites were incubated with the host cell monolayer unperturbed for 8 days (Fig 4E). The total area of the host cell monolayer lysed by the TKO is 40% of the wild-type parasite ($p < 0.0001$), indicating significant lower cytolytic efficiency. Thus, regarding the parasite's ability to move helically or conoid structure, the short-distance host cell entry is less sensitive than infection efficiency.

DISCUSSION

The array of cortical microtubules is one of the major features in the cytoskeleton of *Toxoplasma* and other apicomplexan parasites. In *Toxoplasma,* the roots of the cortical microtubules are precisely located at evenly spaced intervals separated by cogwheel-like projections at the circumference of the apical polar ring [14-16]. The cortical microtubules are co-constructed and associated extensively with the inner membrane complex (IMC), guiding its formation during parasite replication [24, 25]. The inhibition of microtubule polymerization in the daughters results in distorted daughter cortex and failed cell division [26-29]. In mature *Toxoplasma*, the cortical microtubules are extraordinarily stable and resistant to drug or cold-temperature treatments that readily depolymerize mammalian microtubules [26, 28, 29]. It was proposed that the cortical microtubules might have various mechanical roles in facilitating parasite motility and invasion [30, 31, 35]. However, the extraordinary stability of these polymers poses a major barrier against directly testing these hypotheses.

Previously, we generated a mutant (Δ*tlap2*Δ*spm1*Δ*tlap3,* a.k.a." TKO") in which the cortical microtubules are destabilized in the mature parasites while continuing to grow in developing daughters [22]. Here, by quantifying the proportion of TKO parasites with different levels of defects in the array of cortical microtubules, we now have a more complete view of the extent of depolymerization in the non-dividing and dividing parasites. We found that 1) ~ 80% of untreated, non-dividing parasites have severely shortened microtubules and 2) the extent of depolymerization in the mature parasite becomes increasingly marked when the daughters start to form, but the development of daughters is not affected. Examining cortical microtubules in the wild-type also revealed a small proportion of mature parasites with shortened cortical microtubules at the end of daughter construction. This suggests that microtubule depolymerization in the mother parasite might be a part of the normal preparation for disassembling maternal structures into components parts for possible recycle in the new generation. The cortical microtubules in mature TKO parasites are likely further sensitized to the depolymerizing activity due to the lack of TLAP2, SPM1, and TLAP3. Remarkably, in the same cell, while the maternal microtubules are destabilized, the daughter microtubules grow normally. This indicates the local nature of this activity, possibly due to either depolymerizing factors specific for the mother parasite and/or stabilizing factors specific for daughter cells.

When treated with low temperature, the cortical microtubules in the TKO parasite can be fully depolymerized [22]. Here we show that this depolymerization is reversible, when the parasite was placed at 37°C after cold-treatment, short cortical microtubules are found concentrated at the apical end of the parasite. This is consistent with the current hypothesis

310 that the apical polar ring is the nucleating center for the cortical microtubules [14-16]. It is
311 tempting to suggest that the nucleation complexes in the apical polar ring in the mature
312 parasite remain active and are capable of re-nucleating new cortical microtubules after
313 complete depolymerization. However, we cannot exclude the possibility that the new growth
314 occurred from short microtubules that remain associated with the apical polar ring, as a small
315 cap of tubulin antibody labeling remains at the apical end even after prolonged cold treatment.
316 If the latter were true, it suggests differential regulation of stability along the length of the
317 cortical microtubules.
318
319 In the 3-D Matrigel, the TKO mutant moves much more linearly than the wild-type
320 parasite, which travels along an irregular helical path. The stable and spirally arranged cortical
321 microtubules, with their extensive interactions with the cortex, could contribute to the helicity of
322 the parasite movement by maintaining non-isotropic cortical properties (e.g. stiffness), and
323 thus biasing the orientation at which the parasite interacts with its environment. In plant cells,
324 the transmembrane cellulose synthesis complex is dynamically coupled to the cortical
325 microtubules via cellulose synthases interacting (CSI1) protein [36]. This results in the co-
326 alignment of the extracellular cellulose fibers with the cortical microtubules on the other side of
327 the plasma membrane. One could imagine that a similar mechanism might be involved in the
328 confinement of the force-generating actomyosin apparatus associated with the inner
329 membrane complex in *Toxoplasma*, although currently a CSI1-like coupler is unknown. The
330 trajectory of the parasite movement might also be affected by the parasite shape. For example,
331 in *Plasmodium berghei,* the knockout of IMC1h, which changes the shape of the ookinete,
332 results in more linear movement [37]. We do not think this is the likely explanation for the
333 change in movement trajectory of the TKO parasite, as the TKO parasite still maintains the
334 crescent shape characteristic of *Toxoplasma* (e.g. Video S1). In addition, a number of
335 observations complicate the interpretation of the exact contribution of parasite shape in the
336 trajectory of movement. First, in the IMC1h *Plasmodium* mutant, while the cortical microtubules
337 are still present and have a recognizable twist, they are also disorganized, which makes it
338 difficult to disentangle the individual contributions from changes in parasite shape vs in the
339 organization of the microtubules. Second, while it has been shown that the TKO mutant
340 becomes shorter than the wild-type parasite when treated with low temperature [38], the
341 linearity of the movement of the TKO parasite does not differ significantly with or without
342 prolonged cold-treatment.
343
344 It was proposed that the cortical microtubules act as a spring to store and release
345 energy for helical gliding [31]. However, our data suggest that these microtubules do not
346 appear to act as a link in the energy relay vital for parasite movement. While the TKO mutant
347 does not move helically, it is clearly capable of sustaining long-distance movement even under
348 conditions where the TKO parasites were pre-treated with cold to nearly fully depolymerize the
349 microtubules. Therefore the cortical microtubules do not play a role in maintaining directional
350 long-distance movement. This means other higher-order structures are needed to limit the
351 direction of force generation by the actomyosin complex. Whatever these structures might be,
352 they need to be regularly arranged and stably associated with the parasite cortex. One
353 candidate is the array of inner membrane particles (IMPs), which form periodic rows of IMPs
354 that run the length along the longitudinal axis of the parasite [24]. Supporting this hypothesis,
355 the depletion of a potential IMP component (GAPM1a) in mature parasite results in decreased
356 parasite displacement in the 3-D Matrigel [38]. A subset of the IMP rows co-align with the
357 cortical microtubules. In the GAPM1a mutant, the cortical microtubules are disordered and
358 destabilized, also indicating intimate interaction between the two sets of structures. It is worth

359 noting that, in contrast to the GAPM1a mutant, the net displacement of the TKO parasite is
360 similar to that of the wild-type (Fig 3A). This separation of helicity from sustained parasite
361 movement might be due to the cell-stage dependent nature of the stability of the cortical
362 microtubules in the TKO parasite. The IMC cortex of the parasite is built concomitantly with the
363 cortical micotubules during daughter formation. Because the daughter cortical microtubules
364 grow normally in the TKO parasite, the structures in the IMC also likely form largely normally.
365 Thus, we think that, in the mature TKO parasites, we are seeing mainly the impact of the
366 microtubule destabilization itself, which manifests in the change from helical to linear
367 movement.
368
369 Given the precision by which the cortical microtubules are constructed, the
370 sophisticated suite of associated proteins [15, 21-23], and their extraordinary stability, we had
371 expected that they would provide important mechanical support for the cortex in the mature
372 parasite. To our surprise, the shape of the TKO parasite is not grossly different from the wild-
373 type parasite (e.g. Video S1), and there is also no detectable difference in the behavior of the
374 parasite during host cell entry and egress when the parasite experiences considerable
375 mechanical stress pushing through host cell cortex. This indicates that other cortical structures,
376 such as the inner membrane complex and associated intermediate filament-like network, are
377 more critical as structural support in mature parasites. Notably, the conoid structure mutant,
378 Δ*dcx,* which invades with a much lower efficiency [33], also showed wild-type like behavior
379 during entry. This suggests that host cell entry is considerably less sensitive to the change in
380 the structure of the cortical microtubules and conoid compared with extracellular migration
381 during infection.
382
383 Lastly, TLAP2, SPM1, and TLAP3, the three proteins collectively responsible for the
384 stability of cortical microtubules in mature *Toxoplasma*, have well-conserved orthologs in
385 *Plasmodium* spp [22]. It would be intriguing to determine whether the microtubule stabilizing
386 function of these proteins, and the influence of cortical microtubule stability to parasite
387 movement are also conserved among the apicomplexans. As the cortical microtubules in the
388 developing daughter and the mature TKO parasites display distinct polymerization and
389 depolymerization states, identifying the activities responsible for this maternal-filial distinction
390 will generate insights into how the cortical microtubules of the mother and developing
391 daughters (composed of the same polymer and less than half a micron apart) coexist in distinct
392 biochemical states and how the switch from one state to the other occurs as the daughters
393 become mature.
394
395
396 **MATERIALS AND METHODS**
397
398 *T. gondii mutant strains and host cell cultures*
399
400 Host cell and *T. gondii* tachyzoite parasite cultures were maintained as described previously
401 [15, 22, 34, 39]. The TKO (Δ*tlap2*Δ*spm1*Δ*tlap3*) mutant was generated in [22] and the Δ*dcx*
402 parasite was generated in [33].
403
404 *Temperature treatment of T. gondii for testing microtubule stability*
405
406 Cultures of intracellular parasites growing in HFF cells plated in 3.5-cm glass-bottom dishes
407 (MatTek Corporation, CAT# P35G-1.5-14-C or CAT# P35G-1.5-21-C) were incubated at 7°C
408 for 20, 60, 90 or 120 min in the L15 imaging media, which is Leibovit's L-15 (21083-027,
409 Gibco- Life Technologies, Grand Island, NY) supplemented with 1% (vol/vol) heat-inactivated

410 cosmic calf serum (CCS; SH30087.3; Hyclone, Logan, UT). For recovery, the intracellular
411 parasites incubated at 7°C for 2 hours were subsequently placed at 37°C for 5, 10, 20, 30, 60
412 or 120 min in the L15 imaging media. The samples were then processed for
413 immunofluorescence as described below. Total number of parasites analyzed: 444, 422, 468,
414 423 of TKO and 246, 274, 300, 390 of wild-type cold-treated at 7°C for 20, 60, 90 or 120 min,
415 respectively; 440, 428, 456, 496, 396, 360 of TKO, and 295, 168, 172, 166, 205, 230 of wild-
416 type recovered at 37°C for 5, 10, 20, 30, 60, or 120 min, respectively.
417
418 *Immunofluorescence*
419
420 All immunofluorescence labeling steps were performed at room temperature. For intracellular
421 parasites, *T. gondii*–infected HFF monolayers growing in glass-bottom dishes were fixed in 3%
422 (vol/vol) formaldehyde and 50% (vol/vol) methanol in 0.5X PBS for 15 min, permeabilized in
423 0.5% (vol/vol) Triton X-100 (TX-100) in PBS for 15 min, washed with PBS twice, followed by
424 incubating with the primary antibody (mouse monoclonal anti-acetylated tubulin, 6-11B-1,
425 1:1000, Sigma T6793) and then with the secondary antibody (goat anti-mouse IgG- Alexa
426 Fluor 488, A11029, Molecular Probes) at 1:1000, for 1 hr each. For labeling of the Inner
427 Membrane Complex Protein 1 (IMC1), the samples were subsequently blocked with 1.5% BSA
428 in PBS for 1 hour, then incubated for 1 hour with rabbit anti-IMC1 (a kind gift from Dr. Con
429 Beckers, William Carey University) at 1:1000, and finally with goat anti-rabbit IgG -Alexa Fluor
430 568 (A11036, Molecular Probes) at 1:1000 for 1 hour. The antibodies were diluted in the
431 blocking solution (i.e. 1.5% BSA in PBS).
432
433 *Three-dimensional structured-illumination microscopy*
434
435 Three-dimensional structured-illumination microscopy (3D-SIM) image stacks were collected at
436 z-increments of 0.125 µm using a DeltaVision OMX Flex imaging station (GE Healthcare-
437 Applied Precision). A 60x oil immersion lens (numerical aperture [NA] 1.42) and immersion oil
438 at refractive index 1.520 were used. Structured illumination image reconstructions and 3D
439 projections were processed using the functions and software supplied by the manufacturer.
440
441 *Replication assay*
442
443 The intracellular replication assay was performed as described in [5]. Four independent
444 experiments were performed. In each replicate, the number of parasites in ~ 100 vacuoles was
445 counted for each strain at each time point.
446
447 *Egress assay*
448
449 For induced egress assay, parasites were added to MatTek dishes containing a confluent HFF
450 or BS-C-1 monolayer and grown for ~ 35 hours. Cells were washed once and incubated in 2 ml
451 of L15 imaging media and placed at ~7°C for 1 hr, before being moved to the environmental
452 chamber kept at 37ºC which was then replaced with ~ 2 ml of 5 µM A23187 in L15 imaging
453 media. Images were collected at 37ºC with 1 sec interval for 10 minutes on an Applied
454 Precision Delta Vision imaging station equipped with an environmental chamber.
455
456 *Live invasion assays*
457
458 To analyze the behavior of live parasites during invasion, extracellular parasites were used to
459 infect a MatTek dish with a nearly confluent monolayer of HFF cells. The dishes were
460 incubated on ice for ~10 min to facilitate parasite settling on the host cells. The culture was
461 then imaged at 37°C with 1 sec intervals for 15 min to capture invasion events.

Plaque assays

A total of 50, 100 and 150 freshly harvested parasites were added to each well of 6-well plates with confluent HFF monolayers and grown undisturbed for 8 days at 37°C, then fixed with 70% ethanol for 15 min and stained with 1% (wt/vol) crystal violet in 25% (vol/vol) methanol, rinsed with PBS, air-dried, and imaged.

3-D motility assay and image acquisition

The 3-D motility assay for *Toxoplasma,* originally developed in [3], was carried out as described in [34]. For cold-treated parasites, cultures with intracellular parasites were placed at ~ 7ºC for 2 hr, before harvesting as described in [34]. Parasites were harvested and imaged immediately at 37ºC. For each imaging experiment, 151-181 image stacks were acquired at 1.36 sec intervals. Each stack consisted of 41 optical sections, spaced 1 µm apart in the Z-plane (40 µm stacks), with field of view of 1500x1500 pixels, binning 2x2, with a final dimension of 750 x 750 pixels. Image stacks were acquired from at least ~10 µm above the coverslip. To represent the 3-D DIC images in 2-D format (Fig 2 and Video S1&3), we performed focus-stacking using Fiji by applying the Extended Depth of Field Sobel Projection plugin from [40, 41]

DIC image stacks processing and cell tracking

DIC images were processed using our custom scripts extended from [34]. High contrast images were generated by subjecting the DIC images to 1) a 3-D median filter (footprint nx = ny = nz = 2 px) to reduce noise, 2) a 2-D Laplacian filter to attenuate out-of-focus portions of the cells, and 3) a 3-D gradient filter of Sobel type for edge detection. A dilation and erosion process using a maximum filter followed by a minimum filter (footprint nz = 3 px, nx = ny =13 px) was then applied. 2 pixels from all x and y edges were cropped before tracking to avoid edge artifacts. We implemented the imaging filters using Python 3 to enable GPU-acceleration using the CuPy plugin [42-44]. The TrackMate plugin in Fiji was then used to detect and track the parasites in the processed image stacks [40, 45, 46]. The Difference-of-Gaussian (DoG) detector was employed for spot detection with a diameter of 7 µm. To avoid artifacts associated with edge-effects and out-of-focus signal, we excluded spots detected within the first and last 1 µm of the z-dimension and 3 µm of each of the x and y dimension. The Kalman filter tracker was used to reconstruct the cell tracks, and false reconstructions (i.e., “tracks” between debris or random noise) were filtered out based on quality, track length, and duration. The values for these parameters were determined empirically. The resulting tracks were manually verified and errors such as misdetections and gaps corrected by adding or deleting individual spots. To refine spot positions, we used the TrackMate spot fitting feature to fit 3-D Gaussian with fixed radius on each spot. After conducting a second round of manual verification, we then separated the motile parasite tracks from the non-motile tracks by applying another set of filters based on displacement and speed. The 3-D coordinates of both the non-motile and motile tracks were copied to different comma-separated value text files (.csv) for analysis in R version 4.1.2 in RStudio [47, 48].

Trajectory analysis

We used the R package celltrackR v 1.1.0 and our own custom functions to process and analyze the parasite trajectories [47-49]. The complete list of the rest of the R packages we used for our analysis is at the end of this section. First, the global drifts in the data were corrected according to the workflow developed by [49] and we calculated the drift velocity from

513 the corresponding set of non-motile tracks. Then, non-motile ends (the very start or very end)
514 of the parasite trajectories were trimmed to eliminate biases introduced by the asynchronous
515 nature of the parasite motility. After trimming, only tracks with more than four steps (i.e., five
516 tracking points) were included in the subsequent analysis.
517
518 In Fig 3A, the net displacement is a simple Euclidean distance between the first point
519 and the last point of the trajectories. The run length of the parasite is the total distance traveled
520 between two “pauses”, which we defined as an event when the parasite stops moving for more
521 than 5.4 sec (>= 4 frames). "stop moving" means that when the speed of a step (sub-track of
522 length 1) is lower than a threshold. For each data set, the threshold value was calculated by
523 taking the average step-speed of the non-motile tracks. We removed the track points that
524 correspond to pause events, introducing gaps. The motile segments were then obtained by
525 splitting the tracks around those gaps. The run speed was obtained by dividing the motile
526 segment’s total distance (run length) by its total duration. For Fig 3C, the dispersal ratio was
527 calculated by taking the net displacement of the motile segments and dividing it by the run
528 length, where a value of 1 indicates a completely linear track.
529
530 For analyzing the turning angle (Fig 3C), any stops that were not filtered out before (i.e.,
531 stops that lasted less than 4 frames) and steps with displacement of less than 10% of the
532 parasite body length (~ 0.75 μm) were cut out from the motile segments before splitting into
533 sub-segments. Sub-segments that are less than 3-frames long were excluded from the turning
534 angle analysis, which was done based on [49].
535
536 The pitch length is the height of one complete helical turn, which was quantified as the
537 straight-line distance between the starting and ending points of the turn. These points were
538 identified through visual inspection of the trajectories and parasite orientation in 3-D space for
539 the pitch calculation in Fig 3C.
540
541 The 3-D reconstruction of the processed DIC image stacks, along with the tracks
542 exported from TrackMate (Fig 2C, Fig 3B, Video S1-S4), was done using the 3-D viewer and
543 Track Processor in Icy [50]. Gaussian blur with a sigma of 2 was applied to the processed
544 stacks before Icy rendering.
545
546 The Kruskal-Wallis test was done to compare the groups for all of the track
547 measurements in Fig 3A&C [47]. We used R version 4.1.2 [48] and the following R packages:
548 data.table v. 1.14.6 [51], gridExtra v. 2.3 [52], onewaytests v. 2.7 [53], pracma v. 2.4.2 [54],
549 rmarkdown v. 2.20 [55-57], rstatix v. 0.7.2 [58], scales v. 1.2.1 [59], tidyverse v. 2.0.0 [60].
550
551
552 **Acknowledgments**
553 We thank Dr. John M. Murray for critical discussions and readings of the manuscript, and
554 Melissa Molina for tissue culture support. This study was supported by funding from the
555 National Institutes of Health/National Institute of Allergy and Infectious Diseases (R01-
556 AI132463) awarded to K.H.
557
558
559 **Conflict of Interest Statement**
560 The authors declare that they have no conflict of interest.

561 **Figure Legends**
562
563 **Figure 1. The destabilization of cortical microtubules in mature TKO parasites**
564 **A.** Projections of image stacks acquired by three-dimensional structured illumination
565 microscopy (3D-SIM) of the non-dividing wild-type and TKO parasites. While 100% of the wild-
566 type parasites have the typical spirally arranged full microtubule array, ~79% (±8.5% SEM) of
567 the TKO parasites have significantly curtailed/short microtubules. The cortical microtubules are
568 sparse in the rest 21%. Green: tubulin labeling by a mouse anti-acetylated tubulin antibody,
569 which also labels the microtubules in the host cell (arrowhead). Red: cortex labeling by a rabbit
570 anti-IMC1 antibody.
571 **B.** Diagrams of wild-type parasites at the initiation (INT), elongation (EL), pre-emergence (pre-
572 EM), and emergence (EM) stages of daughter construction. Cortical microtubules and the
573 conoid are shown for the mother and daughter parasites.
574 **C.** *Left*: Projections of 3D-SIM images of the TKO and wild-type parasites at the initiation,
575 elongation, pre-emergence, and emergence stage of daughter construction. Hollow arrow:
576 cortical microtubules in the mother parasite. Arrow: daughter parasites. Arrowhead: host cell
577 microtubules. Insets (0.7X) are projections that include a subset of the image stack (sub pj) to
578 better display the structure of the daughter parasites, which are obscured in the full projections
579 (full pj) for the wild-type parasites due to the cortical microtubules in the mother. Note that for
580 the TKO parasite, due to the shortness or complete absence of the maternal microtubules, the
581 daughters are as fully visible in the full projection as in the subset projection.
582 *Right*: Quantification of the proportions of wild-type (top) and TKO (bottom) parasites that
583 display various characteristics in the array of cortical microtubules at different stages, including
584 the non-dividing (non-DIV) stage or the initiation (INT), elongation (EL), pre-emergence (pre-
585 EM), and emergence (EM) stages of daughter construction. For the TKO parasites, the two
586 patterns observed are "short or sparse" (*i.e.* similar to non-dividing TKO parasite) and "absent".
587 For the wild-type parasites, the two patterns observed are "non-dividing wild-type-like" or "short
588 or sparse". Error bars: standard error from three independent experiments. Total number of
589 parasites analyzed: 88, 68, 50, 36 of TKO and 52, 62, 54, 49 of wild-type at the initiation,
590 elongation, pre-emergence, or emergence stage, respectively. The data for the non-dividing
591 stage is the same as shown in Fig 1A.
592 **D.** Average number of cell divisions at 12, 24 or 36 hrs after infection in four independent
593 experiments for RH*Δhx* (*WT*) and TKO parasites. Error bars: standard deviation
594 **E.** *Left*: Quantification of the percentage of non-dividing wild-type and TKO parasites that
595 display various characteristics in the array of the cortical microtubules after being placed at ~
596 7°C for 0, 20, 60, 90 or 120 min (C0-C120) as well as after recovery at 37°C for 5, 10, 20, 30,
597 60, or 120 min after 120 min of ~ 7°C incubation (R5-R120). For the TKO parasites, the two
598 patterns observed are "short or sparse" or "absent". For wild-type parasites, the cortical
599 microtubules remain similar to those in untreated parasites under all conditions tested here
600 (after cold-treatment and cold-treatment plus 37°C recovery). Error bars: standard error from
601 three independent experiments. *Middle*: projection of 3D-SIM images of TKO parasites in
602 which cortical microtubules are absent. *Right*: projection of 3D-SIM images of TKO parasites
603 after 1hr of 37°C (R60) recovery, in which short cortical microtubules at the apical end are
604 seen. Arrowhead: host cell microtubules.
605
606 **Figure 2.** Workflow for image processing and automatic tracking of 3-D motility data acquired
607 by DIC imaging
608 **A.** Schematic diagram of the image processing (red outline and box), detection and tracking
609 (blue outline), and tracks analysis (black outline) workflow for 3-D motility data acquired by DIC

610 imaging. (Red) A representative area of a slice from a DIC image stack before processing and
611 the resulting images corresponding to the filters applied on each processing step using
612 Python3, showing the resulting high contrast image. For details, see Materials and Methods
613 section.
614 **B.** Focused composite image of a DIC image stack (41 slices; 40 *μ*m) of extracellular wild-type
615 parasites in Matrigel and corresponding processed image (represented by its maximum
616 projection) (see also Video S1).
617 **C.** Examples of 3-D tracks for motile RH*Δhx* parental, TKO, RH*Δku80* parental and *Δdcx*
618 parasites reconstructed in the Icy software (see also Video S1- S4). Length of arrow = 16 μm.
619
620 **Figure 3** The 3-D trajectories of TKO parasites are significantly more linear than those of
621 parental parasites.
622 **A.** Frequency distribution and statistical analysis of motion-related parameters including net
623 displacement, run length (distance between pauses >5.4 sec), and run speed of RH*Δhx*
624 parental, TKO, RH*ΔhxΔku80* parental and *Δdcx* parasites. The mean values for individual
625 histograms are shown (in red) and also marked by the red dashed line. ns: p-value not
626 significant. P-values were calculated by the Kruskal-Wallis test.
627 **B.** Representative tracks projected on the (x, y) plane for RH*Δhx* parental, TKO and cold-
628 treated TKO, RH*Δku80* parental and *Δdcx* parasites with superimposed origins (red circles).
629 For cold-treated TKO, intracellular parasite cultures were placed at 7 degree for two hours
630 before harvesting and mixed with Matrigel. For the other samples/conditions, the parasites
631 were harvested as described previously in [34]. All motility assays were carried out at 37°C.
632 Bottom right: enlarged insets (~ 6X) that include the segment indicated by the dashed boxes in
633 the trajectories for RH*Δhx* parental, TKO and cold-treated (CT) TKO parasites.
634 **C.** Frequency distribution and statistical analysis of helical curve-related parameters including
635 turning angle, dispersal ratio, and the pitch of helical turn of RH*Δhx* parental, and TKO, with an
636 illustration defining pitch. Data for all parameters are also displayed for RH*Δku80* parental and
637 *Δdcx* parasites except for the pitch. The mean values for individual histograms are shown (in
638 red) and also marked by the red dashed line. *p<0.05; ****p<0.0001. p values were calculated
639 by the Kruskal-Wallis test.
640
641 **Figure 4.** The speeds of entry and egress of TKO parasites are similar to those of parental
642 parasites despite lower plaquing efficiency
643 **A.** Images selected from time-lapse experiments of intracellular RH*Δhx* parental and TKO
644 parasite treated with 5 μM A23187 (also see Video S5). Parasitophorous vacuoles are
645 indicated by the orange arrows.
646 **B.** Dot plots of time taken to disperse after treatment with 5 μM A23187. The intracellular wild-
647 type and TKO parasite cultures were placed at ~ 7°C for 1 hr prior to the egress experiment,
648 which was conducted at 37°C. Error bars: standard error.
649 **C.** Images selected from time-lapse recording of RH*Δhx* parental, TKO, RH*Δku80* parental and
650 *Δdcx* parasites in the process of invasion (also see Video S6). Frames marked in yellow: entry
651 completed. Green arrows: constrictions formed during invasion.
652 **D.** Dot plots of time taken for entry (i.e. time from parasite contact with the host cell at its apical
653 end to completion of entry) for RH*Δhx* parental, TKO, RH*ΔhxΔku80* parental and *Δdcx*
654 parasites. Error bars: standard error.
655 **E.** *Top*: Plaques formed by the RH*Δhx* parental and TKO parasites. “plaques” are areas of the
656 host cell culture lysed by repeated cycles of parasite invasion, replication, and egress. The
657 cultures were fixed with 70% ethanol and stained with crystal violet 8 days after inoculation.
658 *Bottom*: Bar graphs that compare the number of plaques (left) and total plaque area (right) of

659 the RH*Δhx* parental and TKO parasites. Five independent experiments were conducted. Error
660 bars: standard error. **p<0.01; ****p<0.0001. p values were calculated by unpaired Student's t-
661 tests.
662
663
664

Table 1. Fraction of motile parasites in 3-D motility assay

Parasite strain	*Mean percent motile ± SEM (# of independent replicates)*	*Total number of parasites analyzed*
RH*Δhx* (TKO parental)	40.2 ± 6.36 (*N=6*)	413
TKO	42.3 ± 6.77 (*N=6*)	395
RH*Δhx*Δ*ku80* (Δ*dcx* parental)	36.5 ± 4.00 (*N=8*)	404
Δ*dcx*	30.9 ± 4.97 (*N=9*)	486

665
666
667 **Supplemental Videos:**
668
669
670 **Video S1:** Time-lapse microscopy of 3-D motility in 50% Matrigel for the RH*Δhx* (RH parental
671 1) and TKO parasites. *Left:* Videos of projected DIC images (projections of 3-D stack
672 generated by Stack focuser in ImageJ/Fiji). *Right:* Corresponding processed images with a
673 subset of 3-D trajectories. Time interval: ~ 1.36 sec. Video speed: 10 frames/s.
674
675 **Video S2:** Rotational view of 3-D trajectories for the RH*Δhx* (RH parental 1) and TKO
676 parasites included in Video S1. The traveling sphere associated with each track represents the
677 centroid of the parasite traveling along that path. Length of arrow= 16 μm
678
679 **Video S3:** Time-lapse microscopy of 3-D motility in 50% Matrigel for the RH*Δku80* (RH
680 parental 2) and *Δdcx* (*dcx KO*) parasites. *Left:* Videos of projected DIC images (projections of
681 3-D stack generated by Stack focuser in ImageJ/Fiji). *Right:* Corresponding processed images
682 with a subset of 3-D trajectories. Time interval: ~ 1.36 sec. Video speed: 10 frames/s.
683
684 **Video S4:** Rotational view of 3-D trajectories for the RH*Δku80* (RH parental 2) and *Δdcx* (*dcx*
685 *KO*) parasites included in Video S3. The traveling sphere associated with each track
686 represents the centroid of the parasite traveling along that path. Length of arrow= 16 μm
687
688 **Video S5:** Time-lapse microscopy of A23187 induced-egress for RH*Δhx* (RH parental) and
689 TKO parasites. A23187 was added at the beginning of the movies to a final concentration of 5
690 μM. The intracellular wild-type and TKO parasite cultures were placed at 7°C for 1 hr prior to
691 the egress experiment, which was conducted at 37°C. Time interval: 1 sec. Video speed: 60
692 frames/s. Scale bar: 5 μm.
693
694 **Video S6:** Time-lapse microscopy of host cell entries for RH*Δhx* (RH parental 1), TKO and
695 RH*Δku80* (RH parental 2) and *Δdcx* (*dcx KO*) parasites. Fig 4C includes images selected from
696 the timelapses in the leftmost column. Time interval: 1 sec. Video speed: 6 frames/s. Scale
697 bar: 5 μm.
698

699 **REFERENCES**

700 1. World-Health-Organization, *World Malaria Report 2022.* 2022: p. 293.
701 2. Dubey, J.P., *The history of Toxoplasma gondii--the first 100 years.* The Journal of
702 eukaryotic microbiology, 2008. **55**(6): p. 467-75.
703 3. Leung, J.M., M.A. Rould, C. Konradt, C.A. Hunter, and G.E. Ward, *Disruption of*
704 *TgPHIL1 alters specific parameters of Toxoplasma gondii motility measured in a*
705 *quantitative, three-dimensional live motility assay.* PloS one, 2014. **9**(1): p. e85763.
706 4. Dobrowolski, J.M., V.B. Carruthers, and L.D. Sibley, *Participation of myosin in gliding*
707 *motility and host cell invasion by Toxoplasma gondii.* Mol Microbiol, 1997. **26**(1): p. 163-
708 73.
709 5. Heaslip, A.T., M. Nishi, B. Stein, and K. Hu, *The motility of a human parasite,*
710 *Toxoplasma gondii, is regulated by a novel lysine methyltransferase.* PLoS Pathog,
711 2011. **7**(9): p. e1002201.
712 6. Meissner, M., D. Schluter, and D. Soldati, *Role of Toxoplasma gondii myosin A in*
713 *powering parasite gliding and host cell invasion.* Science, 2002. **298**(5594): p. 837-40.
714 7. Gaskins, E., S. Gilk, N. DeVore, T. Mann, G. Ward, and C. Beckers, *Identification of the*
715 *membrane receptor of a class XIV myosin in Toxoplasma gondii.* J Cell Biol, 2004.
716 **165**(3): p. 383-93.
717 8. Graindorge, A., K. Frenal, D. Jacot, J. Salamun, J.B. Marq, and D. Soldati-Favre, *The*
718 *Conoid Associated Motor MyoH Is Indispensable for Toxoplasma gondii Entry and Exit*
719 *from Host Cells.* PLoS Pathogens, 2016. **12**(1): p. e1005388.
720 9. Jacot, D., N. Tosetti, I. Pires, J. Stock, A. Graindorge, Y.F. Hung, et al., *An*
721 *Apicomplexan Actin-Binding Protein Serves as a Connector and Lipid Sensor to*
722 *Coordinate Motility and Invasion.* Cell Host & Microbe, 2016. **20**(6): p. 731-743.
723 10. Huynh, M.-H. and V.B. Carruthers, *Toxoplasma MIC2 is a major determinant of invasion*
724 *and virulence.* PLoS Pathogens, 2006. **2**(8): p. e84.
725 11. Huynh, M.H., K.E. Rabenau, J.M. Harper, W.L. Beatty, L.D. Sibley, and V.B. Carruthers,
726 *Rapid invasion of host cells by Toxoplasma requires secretion of the MIC2-M2AP*
727 *adhesive protein complex.* Embo J, 2003. **22**(9): p. 2082-90.
728 12. Frenal, K., V. Polonais, J.B. Marq, R. Stratmann, J. Limenitakis, and D. Soldati-Favre,
729 *Functional dissection of the apicomplexan glideosome molecular architecture.* Cell Host
730 Microbe, 2010. **8**(4): p. 343-57.
731 13. Tosetti, N., N. Dos Santos Pacheco, D. Soldati-Favre, and D. Jacot, *Three F-actin*
732 *assembly centers regulate organelle inheritance, cell-cell communication and motility in*
733 *Toxoplasma gondii.* eLife, 2019. **8**: p. e42669.
734 14. Morrissette, N.S. and L.D. Sibley, *Cytoskeleton of apicomplexan parasites.* Microbiol
735 Mol Biol Rev, 2002. **66**(1): p. 21-38.
736 15. Leung, J.M., Y. He, F. Zhang, Y.C. Hwang, E. Nagayasu, J. Liu, et al., *Stability and*
737 *function of a putative microtubule organizing center in the human parasite Toxoplasma*
738 *gondii.* Molecular Biology of the Cell (Featured as Journal Cover), 2017. **28**(10): p.
739 1361-1378.
740 16. Nichols, B.A. and M.L. Chiappino, *Cytoskeleton of Toxoplasma gondii.* J. Protozool.,
741 1987. **34**(2): p. 217-26.
742 17. Wang, X., P. Qian, H. Cui, L. Yao, and J. Yuan, *A protein palmitoylation cascade*
743 *regulates microtubule cytoskeleton integrity in Plasmodium.* The EMBO journal, 2020.
744 **39**(13): p. e104168-e104168.
745 18. Bounkeua, V., F. Li, and J.M. Vinetz, *In vitro generation of Plasmodium falciparum*
746 *ookinetes.* The American journal of tropical medicine and hygiene, 2010. **83**(6): p. 1187-
747 1194.

748 19. Garnham, P.C., R.G. Bird, and J.R. Baker, *Electron microscope studies of motile stages*
749 *of malaria parasites. III. The ookinetes of Haemamoeba and Plasmodium.* Trans R Soc
750 Trop Med Hyg, 1962. **56**: p. 116-20.
751 20. Bannister, L.H. and G.H. Mitchell, *The role of the cytoskeleton in Plasmodium*
752 *falciparum merozoite biology: an electron-microscopic view.* Annals of tropical medicine
753 and parasitology, 1995. **89**(2): p. 105-11.
754 21. Liu, J., L. Wetzel, Y. Zhang, E. Nagayasu, S. Ems-McClung, L. Florens, et al., *Novel*
755 *Thioredoxin-Like Proteins Are Components of a Protein Complex Coating the Cortical*
756 *Microtubules of Toxoplasma gondii.* Eukaryotic cell, 2013. **12**(12): p. 1588-99.
757 22. Liu, J., Y. He, I. Benmerzouga, W.J. Sullivan, Jr., N.S. Morrissette, J.M. Murray, et al.,
758 *An ensemble of specifically targeted proteins stabilizes cortical microtubules in the*
759 *human parasite Toxoplasma gondii.* Molecular Biology of the Cell (Featured as Journal
760 Cover), 2015. **27**(3): p. 549-71.
761 23. Tran, J.Q., C. Li, A. Chyan, L. Chung, and N.S. Morrissette, *SPM1 stabilizes*
762 *subpellicular microtubules in Toxoplasma gondii.* Eukaryot Cell, 2012. **11**(2): p. 206-16.
763 24. Morrissette, N.S., J.M. Murray, and D.S. Roos, *Subpellicular microtubules associate*
764 *with an intramembranous particle lattice in the protozoan parasite Toxoplasma gondii.* J.
765 Cell Sci., 1997. **110**(Pt 1): p. 35-42.
766 25. Hu, K., D.S. Roos, and J.M. Murray, *A novel polymer of tubulin forms the conoid of*
767 *Toxoplasma gondii.* J Cell Biol, 2002. **156**(6): p. 1039-50.
768 26. Morrissette, N.S. and L.D. Sibley, *Disruption of microtubules uncouples budding and*
769 *nuclear division in Toxoplasma gondii.* J Cell Sci, 2002. **115**(Pt 5): p. 1017-25.
770 27. Stokkermans, T.J., J.D. Schwartzman, K. Keenan, N.S. Morrissette, L.G. Tilney, and
771 D.S. Roos, *Inhibition of Toxoplasma gondii replication by dinitroaniline herbicides.* Exp.
772 Parasitol., 1996. **84**(3): p. 355-70.
773 28. Hu, K., J. Johnson, L. Florens, M. Fraunholz, S. Suravajjala, C. DiLullo, et al.,
774 *Cytoskeletal components of an invasion machine – the apical complex of Toxoplasma*
775 *gondii.* PloS pathogens, 2006. **2**(2): p. 0121-0139.
776 29. Hu, K., *Organizational Changes of the Daughter Basal Complex during the Parasite*
777 *Replication of Toxoplasma gondii.* PLoS Pathogens, 2008. **4**((1)): p. 108-121.
778 30. Stadler, R.V., L.A. White, K. Hu, B.P. Helmke, and W.H. Guilford, *Direct measurement*
779 *of cortical force generation and polarization in a living parasite.* Mol Biol Cell, 2017. **E16-**
780 **07-0518**.
781 31. Pavlou, G., B. Touquet, L. Vigetti, P. Renesto, A. Bougdour, D. Debarre, et al., *Coupling*
782 *Polar Adhesion with Traction, Spring, and Torque Forces Allows High-Speed Helical*
783 *Migration of the Protozoan Parasite Toxoplasma.* ACS Nano, 2020. **14**(6): p. 7121-
784 7139.
785 32. Swedlow, J.R., K. Hu, P.D. Andrews, D.S. Roos, and J.M. Murray, *Measuring tubulin*
786 *content in Toxoplasma gondii: a comparison of laser-scanning confocal and wide-field*
787 *fluorescence microscopy.* Proc Natl Acad Sci U S A, 2002. **99**(4): p. 2014-9.
788 33. Nagayasu, E., Y.-c. Hwang, J. Liu, J. Murray, and K. Hu, *Loss of a doublecortin (DCX)*
789 *domain containing protein causes structural defects in a tubulin-based organelle of*
790 *Toxoplasma gondii and impairs host cell invasion.* Molecular Biology of the Cell, 2016.
791 **E16-08-0587**
792 34. Munera Lopez, J., I.F. Tengganu, J. Liu, J.M. Murray, L.F. Arias Padilla, Y. Zhang, et
793 al., *An apical protein, Pcr2, is required for persistent movement by the human parasite*
794 *Toxoplasma gondii.* PLoS Pathog, 2022. **18**(8): p. e1010776.

35. Del Rosario, M., J. Periz, G. Pavlou, O. Lyth, F. Latorre-Barragan, S. Das, et al., *Apicomplexan F-actin is required for efficient nuclear entry during host cell invasion.* EMBO reports, 2019. **20**(12): p. e48896.
36. Bringmann, M., B. Landrein, C. Schudoma, O. Hamant, M.T. Hauser, and S. Persson, *Cracking the elusive alignment hypothesis: the microtubule-cellulose synthase nexus unraveled.* Trends Plant Sci, 2012. **17**(11): p. 666-74.
37. Kan, A., Y.-H. Tan, F. Angrisano, E. Hanssen, K.L. Rogers, L. Whitehead, et al., *Quantitative analysis of Plasmodium ookinete motion in three dimensions suggests a critical role for cell shape in the biomechanics of malaria parasite gliding motility.* Cellular Microbiology, 2014. **16**(5): p. 734-750.
38. Harding, C.R., M. Gow, J.H. Kang, E. Shortt, S.R. Manalis, M. Meissner, et al., *Alveolar proteins stabilize cortical microtubules in Toxoplasma gondii.* Nature Communications, 2019. **10**(1): p. 401.
39. Roos, D.S., R.G. Donald, N.S. Morrissette, and A.L. Moulton, *Molecular tools for genetic dissection of the protozoan parasite Toxoplasma gondii.* Methods Cell Biol., 1994. **45**: p. 27-78.
40. Schindelin, J., I. Arganda-Carreras, E. Frise, V. Kaynig, M. Longair, T. Pietzsch, et al., *Fiji: an open-source platform for biological-image analysis.* Nature methods, 2012. **9**(7): p. 676-82.
41. Forster, B., D. Van De Ville, J. Berent, D. Sage, and M. Unser, *Complex wavelets for extended depth‐of‐field: A new method for the fusion of multichannel microscopy images.* Microscopy research and technique, 2004. **65**(1‐2): p. 33-42.
42. Harris, C.R., K.J. Millman, S.J. van der Walt, R. Gommers, P. Virtanen, D. Cournapeau, et al., *Array programming with NumPy.* Nature, 2020. **585**(7825): p. 357-362.
43. Okuta, R., Y. Unno, D. Nishino, S. Hido, and Crissman. *CuPy : A NumPy-Compatible Library for NVIDIA GPU Calculations*. 2017.
44. Van Rossum, G.a.D., Fred L., *Python 3 Reference Manual*. 2009, Scotts Valley, CA, USA: CreateSpace.
45. Tinevez, J.Y., N. Perry, J. Schindelin, G.M. Hoopes, G.D. Reynolds, E. Laplantine, et al., *TrackMate: An open and extensible platform for single-particle tracking.* Methods, 2017. **115**: p. 80-90.
46. Ershov, D., M.-S. Phan, J.W. Pylvänäinen, S.U. Rigaud, L. Le Blanc, A. Charles-Orszag, et al., *TrackMate 7: integrating state-of-the-art segmentation algorithms into tracking pipelines.* Nature Methods, 2022. **19**(7): p. 829-832.
47. RStudioTeam, *RStudio: Integrated Development for R.* RStudio, PBC, Boston, MA 2020. **URL http://www.rstudio.com/**.
48. Team, R.C., *{R}: A Language and Environment for Statistical Computing*, 2021, R Foundation for Statistical Computing: Vienna, Austria.
49. Wortel, I.M.N., A.Y. Liu, K. Dannenberg, J.C. Berry, M.J. Miller, and J. Textor, *CelltrackR: An R package for fast and flexible analysis of immune cell migration data.* ImmunoInformatics, 2021. **1-2**: p. 100003.
50. de Chaumont, F., S. Dallongeville, N. Chenouard, N. Hervé, S. Pop, T. Provoost, et al., *Icy: an open bioimage informatics platform for extended reproducible research.* Nat Methods, 2012. **9**(7): p. 690-6.
51. Dowle, M. and A. Srinivasan, *{data.table}: Extension of '{data.frame}'*, 2022.
52. Auguie, B., *{gridExtra}: Miscellaneous Functions for "{Grid}" Graphics*, 2017.
53. Dag, O., A. Dolgun, and N.M. Konar, *{onewaytests: An R Package for One-Way Tests in Independent Groups Designs}.* {The R Journal}, 2018. **10**(1): p. 175-199.
54. Borchers, H.W., *{pracma}: Practical Numerical Math Functions*, 2022.

55. Allaire, J.J., Y. Xie, J. McPherson, J. Luraschi, K. Ushey, A. Atkins, et al., *{rmarkdown}: Dynamic Documents for R*, 2023.
56. Xie, Y., J.J. Allaire, and G. Grolemund, *R Markdown: The Definitive Guide*. 2018, Boca Raton, Florida: Chapman and Hall/CRC.
57. Xie, Y., C. Dervieux, and E. Riederer, *R Markdown Cookbook*. 2020, Boca Raton, Florida: Chapman and Hall/CRC.
58. Kassambara, A., *{rstatix}: Pipe-Friendly Framework for Basic Statistical Tests*, 2023.
59. Wickham, H. and D. Seidel, *{scales}: Scale Functions for Visualization*, 2022.
60. Wickham, H., M. Averick, J. Bryan, W. Chang, L.D.A. McGowan, R. François, et al., *Welcome to the {tidyverse}.* Journal of Open Source Software, 2019. **4**(43): p. 1686.

Figure 1

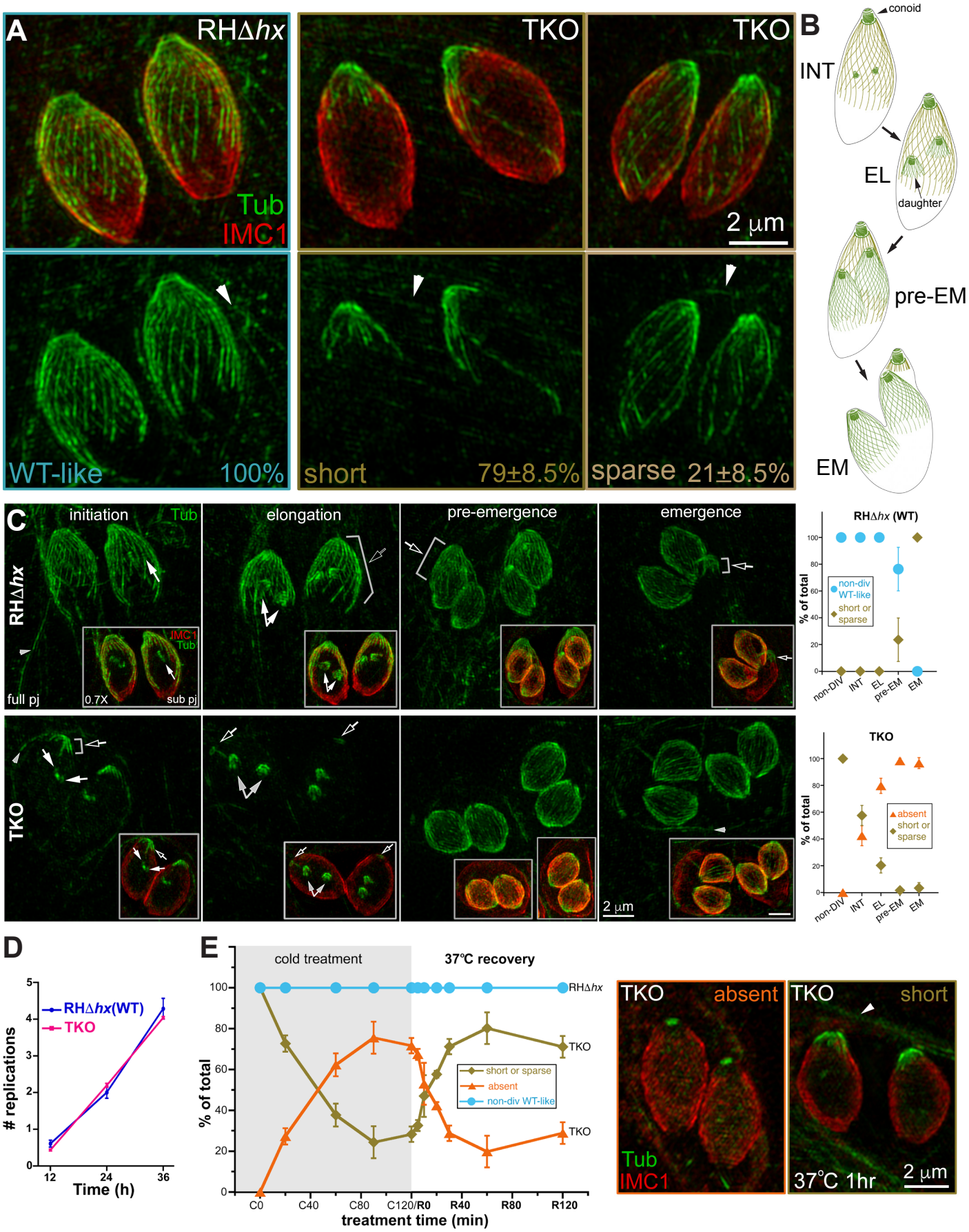
A
RHΔhx
TKO
TKO
Tub
IMC1
2 μm
WT-like
100%
short
79±8.5%
sparse
21±8.5%
B
conoid
INT
EL
daughter
pre-EM
EM
C
initiation
Tub
elongation
pre-emergence
emergence
RHΔhx
JMC1
Tub
full pj
0.7X
sub pj
TKO
2 μm
RHΔhx (WT)
% of total
non-div WT-like
short or sparse
non-DIV
INT
EL
pre-EM
EM
TKO
absent
short or sparse
D
RHΔhx(WT)
TKO
replications
Time (h)
E
cold treatment
37°C recovery
RHΔhx
TKO
short or sparse
absent
non-div WT-like
% of total
C0
C40
C80
C120/R0
R40
R80
R120
treatment time (min)
TKO
absent
Tub
IMC1
TKO
short
37°C 1hr
2 μm

Figure 2

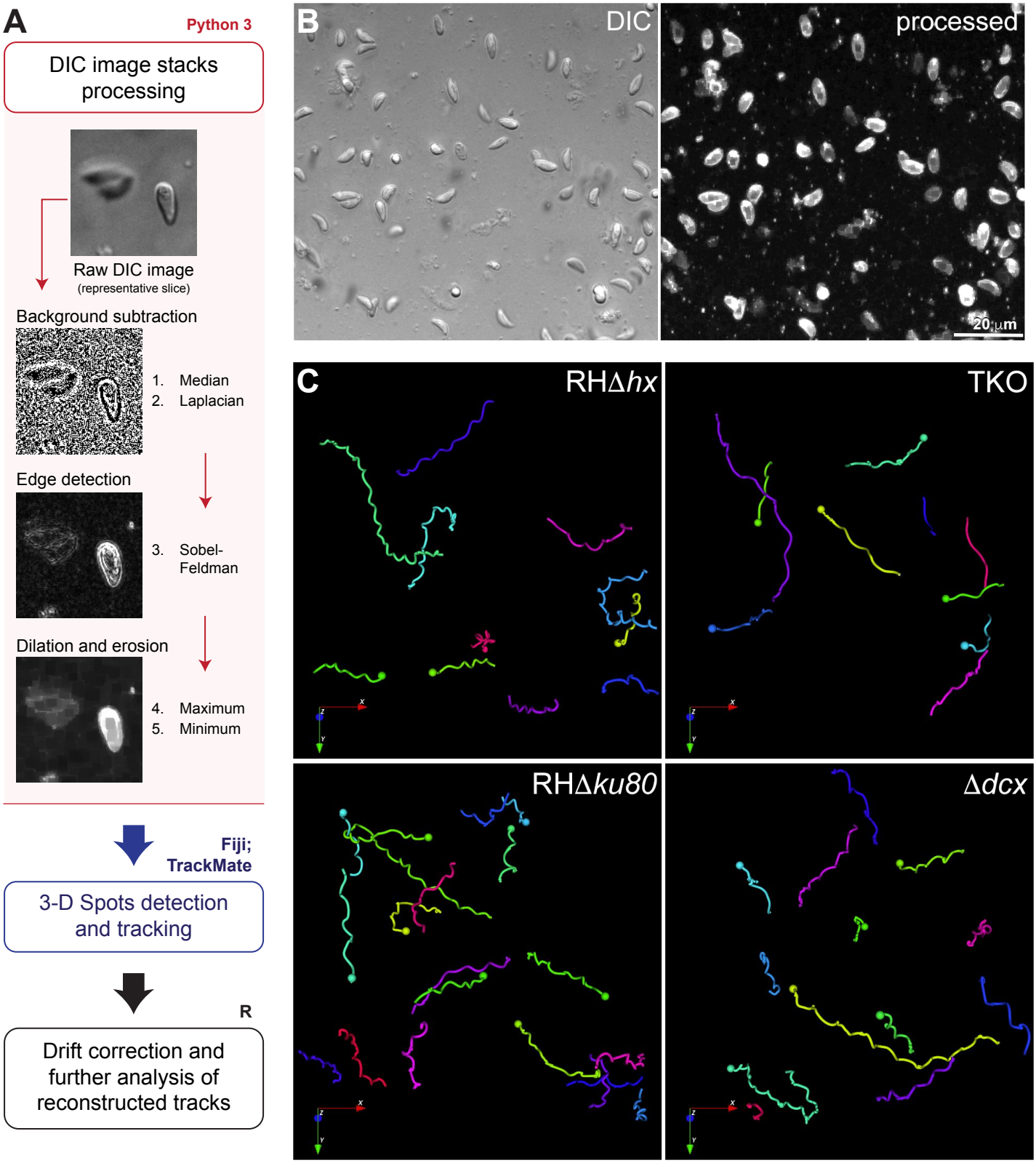
A
Python 3
DIC image stacks processing
Raw DIC image
(representative slice)
Background subtraction
1. Median
2. Laplacian
Edge detection
3. Sobel-Feldman
Dilation and erosion
4. Maximum
5. Minimum
Fiji; TrackMate
3-D Spots detection and tracking
R
Drift correction and further analysis of reconstructed tracks
B
DIC
processed
20 µm
C
RHΔhx
TKO
RHΔku80
Δdcx

Figure 3

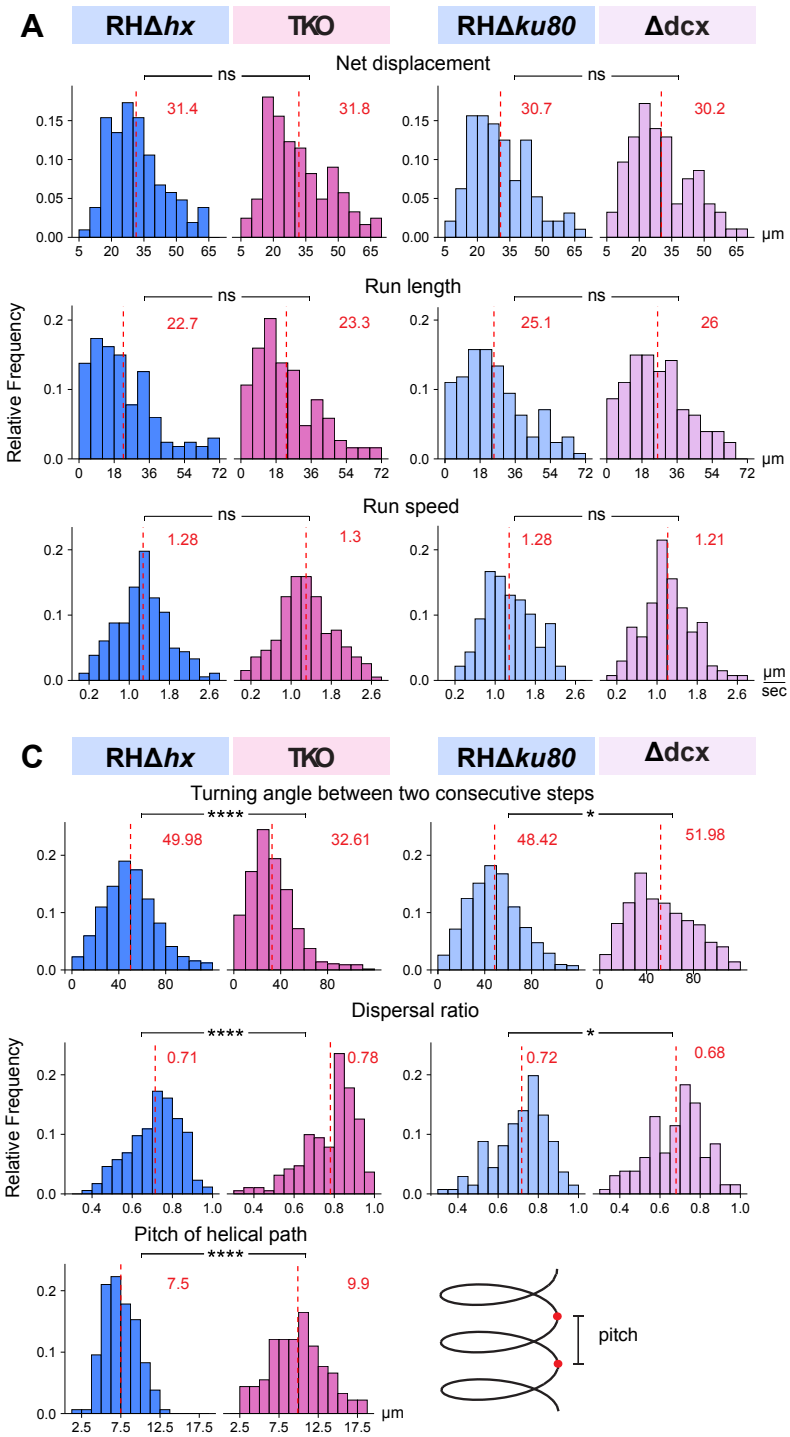
A
RHΔhx
TKO
RHΔku80
Δdcx
Net displacement
ns
31.4
31.8
30.7
30.2
Run length
22.7
23.3
25.1
26
Run speed
1.28
1.3
1.28
1.21
Relative Frequency
μm
μm/sec
C
Turning angle between two consecutive steps
****
*
49.98
32.61
48.42
51.98
Dispersal ratio
0.71
0.78
0.72
0.68
Pitch of helical path
7.5
9.9
pitch

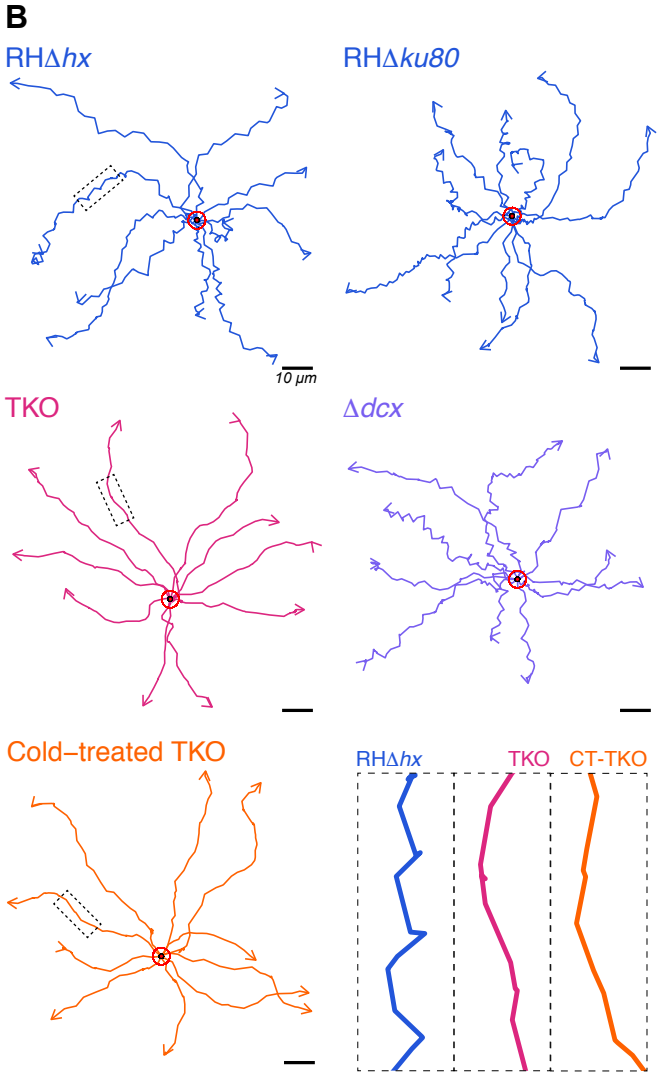
B
RHΔhx
RHΔku80
10 μm
TKO
Δdcx
Cold–treated TKO
RHΔhx
TKO
CT-TKO

Figure 4

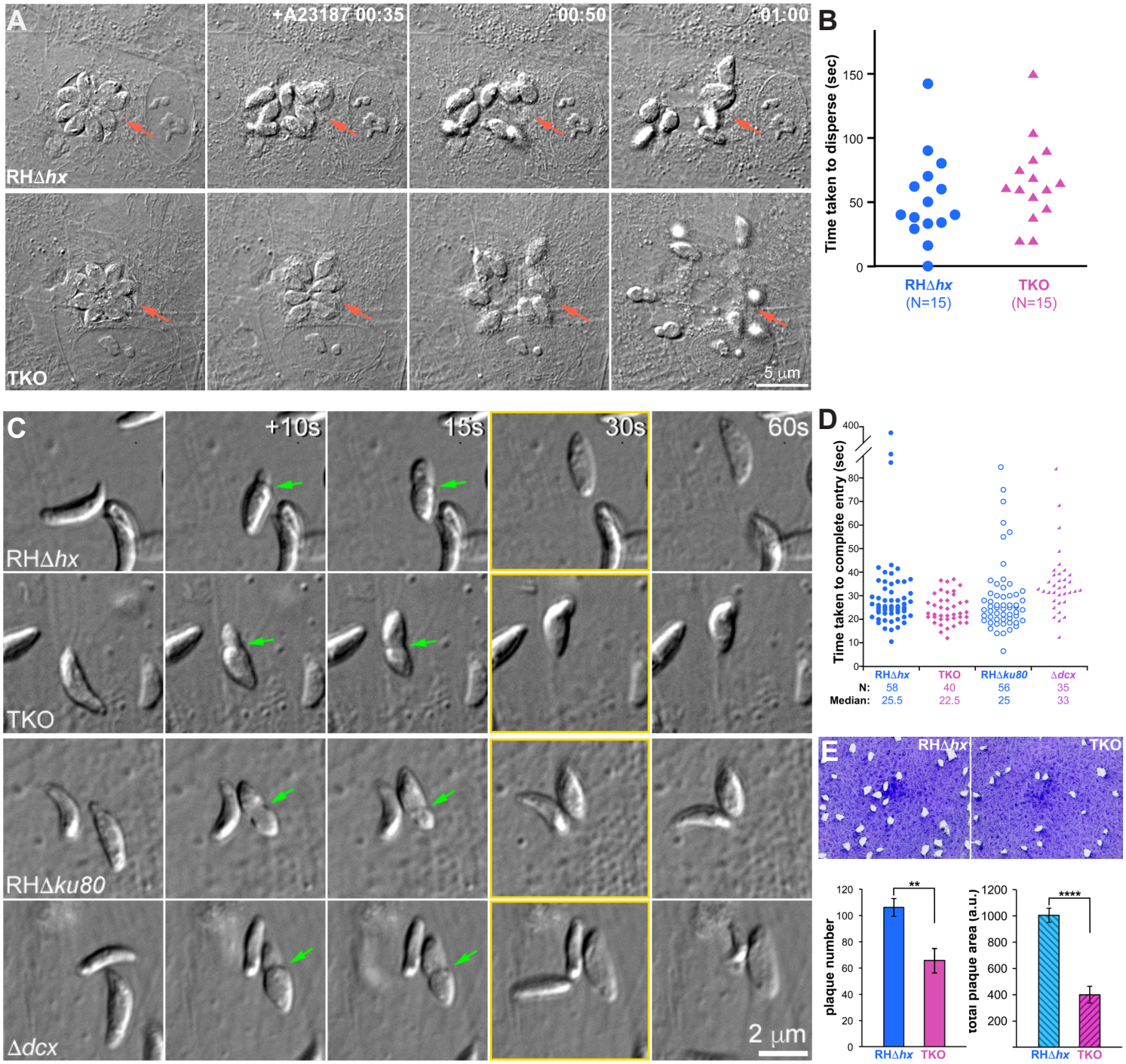
A
+A23187 00:35
00:50
01:00
RHΔhx
TKO
5 µm
B
Time taken to disperse (sec)
150
100
50
0
RHΔhx
(N=15)
TKO
(N=15)
C
+10s
15s
30s
60s
RHΔhx
TKO
RHΔku80
Δdcx
2 µm
D
Time taken to complete entry (sec)
400
80
70
60
50
40
30
20
10
0
RHΔhx
TKO
RHΔku80
Δdcx
N:
58
40
56
35
Median:
25.5
22.5
25
33
E
RHΔhx
TKO
plaque number
120
100
80
60
40
20
0
**
RHΔhx
TKO
total plaque area (a.u.)
1200
1000
800
600
400
200
****
RHΔhx
TKO